Nickel Metal Nanoparticles as Anode Electrocatalysts for Highly Efficient Direct Borohydride Fuel Cells

Alexandr Oshchepkov, Guillaume Braesch, Salem Ould-Amara, Gholamreza Rostamikia, Gaël Maranzana, Antoine Bonnefont, Vasiliki Papaefthimiou, Michael Janik, Marian Chatenet, Elena R. Savinova

Nickel Metal Nanoparticles as Anode Electrocatalyst for Highly-Efficient Direct Borohydride Fuel Cells

Alexandr G. Oshchepkov[†,‡,], Guillaume Braesch[†,§], Salem Ould-Amara[‖], Gholamreza Rostamikia[⊥], Gaël Maranzana[‖], Antoine Bonnefont[#], Vasiliki Papaefthimiou[†], Michael J. Janik[⊥], Marian Chatenet[§,*], Elena R. Savinova[†]*

[†] Institut de Chimie et Procédés pour l'Energie, l'Environnement et la Santé, UMR 7515 CNRS-University of Strasbourg, 67087 Strasbourg Cedex, France

[‡] Boreskov Institute of Catalysis, 630090 Novosibirsk, Russia

[§] University Grenoble Alpes, University Savoie Mont Blanc, CNRS, Grenoble INP, LEPMI, 38000 Grenoble, France

[‖] Université de Lorraine, CNRS, LEMTA, UMR 7563, 54504 Vandoeuvre Les Nancy, France

[⊥] Department of Chemical Engineering, Pennsylvania State University, University Park, PA, 16802, USA

[#] Institut de Chimie de Strasbourg, UMR 7177 CNRS-University of Strasbourg, 67070 Strasbourg, France

KEYWORDS. Borohydride Oxidation Reaction (BOR), Direct Borohydride Fuel Cell (DBFC), Nickel, Platinum, Palladium, Density Functional Theory (DFT)

ABSTRACT. Developing cost-effective electrocatalysts for the multi-electron borohydride oxidation reaction (BOR) is mandatory to deploy direct borohydride fuel cell (DBFC) systems to power portable and mobile devices. Currently DBFCs rely on noble metal electrocatalysts, and are not capable to fully profit from the high theoretical DBFC voltage, due to the competing hydrogen evolution reaction. Here, highly-efficient noble metal-free BOR electrocatalysts based on carbon-supported Ni nanoparticles considerably outperform Pt/C at overpotentials as low as 0.2 V, both in half-cell and in unit fuel cell configurations. Precise control of the oxidation state of surface Ni is determines the electrocatalytic activity. Density functional theory (DFT) calculations ascribe the exceptional activity of Ni compared to Pt, Pd or Au to a better balance in the adsorption energies of H_{ad}, OH_{ad} and B-containing reactive intermediates. These new findings suggest design principles for efficient noble metal-free BOR electrocatalysts for DBFCs.

INTRODUCTION

Sodium borohydride ($NaBH_4$) is a promising carbon-free energy carrier, owing to its high energy density, non-toxicity, facile storage and transportation (in liquid or solid form), and wide availability [1]. BH_4^- can be directly used as a fuel in direct borohydride fuel cells (DBFCs), by feeding base-stabilized $NaBH_4$ solution to the anode [2], where the borohydride oxidation reaction (BOR) occurs:

$$BH_4^- + 8\,OH^- \rightarrow BO_2^- + 6\,H_2O + 8\,e^- \qquad E^0 = -0.41\ V\ vs\ RHE \qquad (1)$$

Alternatively, $NaBH_4$ can be used as a source of hydrogen, which can be released upon reaction with water (Equations 1, 2) and further used in a hydrogen-fed fuel cell, e.g. a proton exchange membrane FC (PEMFC).

$$BH_4^- + H_2O \rightarrow BH_3OH + H_2 \qquad (2)$$

$$BH_3OH + H_2O \rightarrow BO_2^- + 3\,H_2 \qquad (3)$$

Compared to state-of-the-art PEMFCs, DBFCs exhibit high theoretical open-circuit voltage (1.64 V for a DBFC *vs*. 1.23 V for a PEMFC), and are compatible with non-noble metals, while platinum-group metal (PGM) electrocatalysts are typically required in PEMFCs. This makes DBFCs a competitive alternative to PEMFCs for mobile and portable applications, where high energy-density is targeted.

However, state-of-the-art DBFCs are currently using PGM electrocatalysts, at least at one of their electrodes [3,4], and cannot deliver an open-circuit voltage exceeding that of PEMFCs, due to the competing faradaic hydrogen evolution reaction (HER, Equation 4), which occurs at low anode potentials, and to the non-faradaic heterogeneous hydrolysis of BH_4^- (Equations 2, 3). These processes result in hydrogen escape [4–6] and a decrease of the faradaic efficiency of the fuel conversion.

$$2\,H_2O + 2\,e^- \rightarrow 2\,OH^- + H_2 \qquad E^0 = 0\ V\ vs\ RHE \qquad (4)$$

The competition between BOR, HER, and borohydride hydrolysis depends on: (i) the composition of the electrocatalyst and (ii) the anode potential. High anode overpotentials favor BOR kinetics (unless the electrocatalyst is poisoned by reaction intermediates or passivated by oxides [5–7]) but are of little practical interest. The strength of BH_4^- adsorption and thus the electrocatalytic activity depend on the nature of the catalytic material. Noble metals like Pt, Pd, Ir, *etc.* [8], strongly adsorb BH_4^-, resulting in its dissociation and formation of $BH_{x,ad}$ and (4-*x*) H_{ad}. However, high electrocatalytic activity of PGMs in the HER as well as intensive hydrolysis of borohydride on these materials result in BOR overpotentials above 0.4 V, a severe drawback for the practical energetic efficiency of a DBFC. Molecular adsorption of $BH_{4,ad}$ with much less favorable adsorption energy was proposed for Au, Ag and Cu [8,9]. These metals, being in theory more selective for the direct BOR, with a very low rate of borohydride hydrolysis [10,11], however, show poor activity towards the BOR, owing to their inability to activate B-H bond breaking.

Nickel is a popular material for a variety of electrochemical applications in alkaline media, owing to its low cost, high availability and high corrosion stability: Ni is used in various energy storage/conversion systems, e.g. batteries and electrochemical capacitors [12–17], as well as to electrocatalyze oxygen evolution/reduction reactions [18–23] and hydrogen evolution/oxidation reactions (HER/HOR) [24–27]. However, the literature remains very uncertain regarding the activity of Ni towards the BOR: some papers point to low activity [28–30], whereas others suggest the BOR to proceed already at relatively low overpotentials [31–34]. As of today, no electrocatalyst that enables both high BOR rate, high faradaic efficiency and low BOR onset potential has been isolated with certitude.

Here we propose design principles for highly-active BOR electrocatalysts enabling the reaction to proceed at relatively low overpotentials and outperforming all currently-known materials. We capitalize on the strong dependence of the HER electrocatalysis on the extent of the oxidation of the Ni surface [25,35] and demonstrate that by controlling the surface state of Ni, it is possible to suppress the competing HER and enable fast BOR at potentials below 0 V *vs* RHE. Ni_{ED}/C electrocatalysts are prepared by electrodeposition and compared with commercially-available Pt/C, Pd/C, Au/C electrocatalysts (the most studied BOR materials to date) [2,6,36]. The results of this comparison show outstanding performances of Ni_{ED}/C both in half-cell and in unit fuel cell configurations, in terms of activity and stability of the BOR current at low overpotentials. The experimental data are rationalized by using density functional theory (DFT) calculations and comparing adsorption energies of reactive species at various metal surfaces.

MATERIALS AND METHODS

Synthesis of Ni_{ED}/C electrocatalysts. Synthesis of Ni_{ED}/C electrocatalysts was performed by potentiostatic electrodeposition from a 0.01 M $NiSO_4$ + 0.10 M $(NH_4)_2SO_4$ solution (obtained from $NiSO_4 \cdot 6H_2O$ (99.99%, Aldrich) and $(NH_4)_2SO_4$ (99.0%, Aldrich) granules) at T = 25ºC using porous Vulcan XC-72R carbon (Cabot) as a support following the procedure developed by Oshchepkov et al. [25]. Briefly, a thin layer of XC-72R carbon (*ca.* 100 μg_C cm^{-2}_{geom}) containing 5 wt.% of Nafion was fixed on the surface of a glassy-carbon (GC) disk (Ø 5 mm). The electrodeposition was then performed by using a 2 step sequence: E_{D1} = -0.54 V *vs* RHE (15 s), E_{D2} = -0.29 V *vs* RHE (210 s) while rotating the electrode at ω = 400 rpm (to facilitate removal of hydrogen evolved during electrodeposition). Commercial 40% Pt/XC-72 (Alfa Aesar), 40% Pd/XC-72 and 40% Au/XC-72 (both from Premetek) electrocatalysts were used for comparison.

The Ni_{ED}/C electrocatalyst was fixed on a surface of glassy-carbon disk to make a layer of similar thickness (*ca.* 100 μg_C cm^{-2}_{geom}), containing 5 wt.% of Nafion with respect to the mass of carbon.

Ni_{ED}/GDE anodes were prepared by electrodeposition from the bath containing 0.10 M $NiSO_4$ + 0.10 M $(NH_4)_2SO_4$ on the surface of a carbon cloth (SGL, 4 cm x 2 cm, SIGRATEX®) soaked beforehand in a concentrated HNO_3 solution for 5 min (to improve its hydrophilicity) and thoroughly rinsed by pure water. A three-step electrodeposition procedure with E_{D1} = 0.03 V (10 s), E_{D2} = -0.74 V (15 s), and E_{D3} = -0.54 V *vs* RHE (210 s) was applied once to prepare the Ni_{ED}/GDE-L electrode with low Ni loading, or six times to get the Ni_{ED}/GDE-H electrode with a high Ni loading. In this procedure, the first step was needed to avoid current overload while starting to apply highly negative potential. Typical Ohmic resistance in the electrodeposition bath was measured to be between 2.7 and 3.2 Ohm. The amount of electrodeposited Ni was analyzed by ICP-AES after Ni dissolution from the Ni_{ED}/C and Ni_{ED}/GDE samples in 30 % HNO_3 solution.

Materials characterization. The morphology and the microstructure of Ni_{ED}/C and Ni_{ED}/GDE were studied by STEM (LaB6-JEOL 2100), TEM (JEOL 2100F) and SEM (Zeiss Gemini SEM-500), operating at 200, 200 and 3 kV, respectively. XRD patterns of Ni_{ED}/GDE were recorded on a Bruker D8 Advance diffractometer. XRD patterns of Ni_{ED}/GDE were recorded on Bruker D8 Advance diffractometer. For surface elemental analysis, XPS measurements were performed in an ultra-high vacuum chamber (residual gas pressure < 5 10^{-8} mbar) equipped with a RESOLVE 120 MCD5 hemispherical electron analyzer and a dual anode (Al and Mg Kα) X-ray source. Survey and narrow scan Ni 2p, O 1s, C 1s and B 1s spectra were recorded using Al Kα line (hv = 1486.6 eV). The constant pass energy mode was used to record both survey and high resolution spectra, with pass energies of 100 and 20 eV, respectively. The Binding Energies (BE) of all photoelectron peaks were referenced to the C 1s peak of adventitious carbon (at 284.6 eV). XP spectra were

curve-fitted after Shirley background subtraction following the procedure described in our previous works by deconvolution of the Ni 2p spectra into two peak components (Ni^{2+} and metallic Ni), while the O 1s spectra were fitted using 3 components: adsorbed water (ca. 533.7 eV), surface hydroxyl + alcohol groups (ca. 531.7 eV) and lattice oxygen related to NiO (ca. 529.6 eV) [25,35].

Electrochemical measurements. Electrochemical measurements were carried out in a three-electrode Teflon cell thermostated at $T = 25°C$ with a Pt wire as a counter-electrode and Hg/HgO as a reference electrode ($E_{Hg/HgO} = 0.93$ V *vs* RHE). Although the use of Pt as a counter electrode may cause contamination of the working electrode, for example, when studying hydrogen evolution or oxygen reduction reactions, this should not be an issue when testing BOR electrocatalysts. Indeed, the Pt counter electrode will experience reduction conditions (the HER) and therefore negligibly corrode. Besides, characterization of the Ni_{ED}/C and Ni_{ED}/GDE electrodes either after the synthesis or RDE measurements, confirmed an absence of any sign of Pt contamination (Figures S1-S3). The measurements were performed in 1.0 M NaOH solution (prepared from 50% NaOH solution in water, Premium quality, Aldrich) using either Gamry REF 600 or Autolab PGSTAT302N potentiostats.

After immersion in the electrochemical cell and before the measurement of their electrocatalytic activities, Ni_{ED}/C electrodes were conditioned in N_2-saturated 1 M NaOH by cycling between -0.20 and 0.40 V *vs* RHE at a sweep rate (v) of 20 mV s^{-1}. The cyclic voltammetry (CV) curves acquired afterwards in the potential interval from -0.06 to 0.40 V *vs* RHE were employed to estimate the electrochemical surface area (ECSA) of Ni considering the entire value of the anodic charge and the 0.514 mC cm^{-2} conversion coefficient. The catalytic performance in the BOR was derived from the RDE voltammetric data obtained in N_2-saturated 5 (50) mM $NaBH_4$ + 1.0 M NaOH electrolyte at $\omega = 1600$ rpm. Positive-feedback IR compensation (80 %) was used during

the measurements with typical Ohmic resistance of the electrolyte measured to be between 1 and 5 Ohm.

To perform the XPS measurements, the GC cylinders with Ni_{ED}/C electrocatalysts were pulled out from the electrolyte (either 1 M NaOH or 1 M NaOH + 50 mM $NaBH_4$) at 0 V *vs* RHE (the final scan was stopped when going from negative to positive values), rinsed with water, fixed on the sample holder and protected with a drop of purified water (aiming to minimize the contact with the ambient atmosphere). After that the holder was quickly placed into the entry chamber of the XP spectrometer, degassed down to $P \approx 10^{-5}$ Pa and only then the sample was transferred to the main chamber of the XP spectrometer. Typically, the duration of the transfer procedure did not exceed 5 min.

Fuel cell study. A unit cell with the active electrode surface area of 8 cm^2 developed at LEMTA was used for the DBFC tests. Anodic and cathodic flow fields were single serpentine channels (1 mm width, 0.7 mm deep) machined in a brass block and coated with gold [37]. The membrane electrode assembly was constituted of: (i) an anodic active layer made of either a commercial Pt-black/GDE with a loading of 2 mg_{Pt} cm^{-2} (Fuel Cells Etc) or a Ni_{ED}/GDE with a loading of 0.60 ± 0.05 or 3.6 ± 0.1 mg_{Ni} cm^{-2} for Ni_{ED}/GDE-L and Ni_{ED}/GDE-H, respectively (according to ICP-AES), (ii) a commercial Nafion® NRE-212 membrane exchanged for the Na^+ form, (iii) a commercial air cathode Pt-black/GDE (2 mg_{Pt} cm^{-2}). PTFE seals were used to adjust the thickness of the electrodes to get 20% of compression of the initial thickness. The anodic fuel was composed of 0.5 M $NaBH_4$ in 4.0 M NaOH (VMR Analar® Normapur®). Pure oxygen (Messer, 99.99%) was used at the cathode. No sensitivity to oxygen flow rate was noticed. Temperature regulation was provided thanks to a circulating bath driven by a Pt (100) probe inserted in the anodic plate. Before

entering the cell, the cooling water passed through a heat exchanger, the function of which was to preheat the borohydride solution to the desired temperature.

Computational methods. All calculations were performed using the ab initio total energy and molecular-dynamics Vienna ab initio simulation program (VASP) developed at the Institute for Material Physics at the University of Vienna [38–40]. The projector augmented wave method, Perdew-Wang [41] form of the generalized gradient approximation (GGA) and a cut-off energy of 450 eV were used to represent the electronic structure. A 5×5×1 Monkhorst-Pack k-point grid [42] and spin polarized calculations were used during structural optimizations. Structural optimization minimized the forces on all atoms to less than 0.02 eV $Å^{-1}$. Harmonic vibrational modes were calculated to determine the zero-point vibrational energy (ZPVE) corrections to the total energy of adsorbed species and isolated molecules. The Ni(111) surface was modeled using a 3×3, four layer slab with the bottom two layers constrained to the Ni face centered cubic (fcc) lattice positions. A vacuum region of 15 Å was inserted between the slabs.

RESULTS AND DISCUSSION

BOR activity of Ni_{ED}/C *vs.* its surface state. Ni_{ED}/C electrocatalysts synthesized by electrodeposition of Ni on Vulcan XC-72R were characterized by scanning transmission electron microscopy (STEM); STEM revealed formation of metal nanoparticles with a mean size of *ca*. 10 nm, homogeneously distributed over the support surface (Figures 1a-c). The estimated interplanar spacing of 0.205 nm corresponds to the (111) plane of Ni (0.2034 nm, calculated for a theoretical lattice constant a = 0.35238 nm for crystalline Ni [ICDD PDF-2#00-004-0850]). Ni content was estimated as *ca*. 40 wt.% by inductively-coupled plasma atomic emission spectroscopy (ICP-AES).

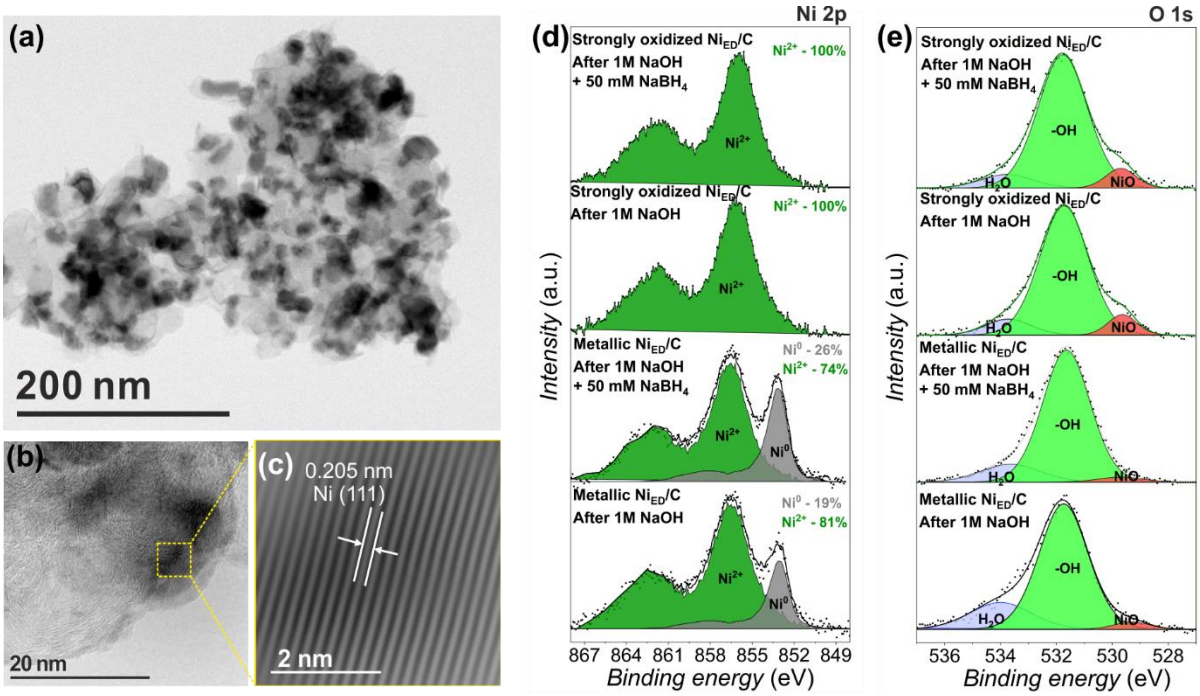

Figure 1. (a) Low and (b) high-resolution STEM images of the as-prepared Ni_{ED}/C electrocatalyst, (c) FFT-filtered magnified area highlighted in the dashed box in (b); *ex situ* X-Ray photoelectron (d) Ni $2p_{3/2}$ and (e) O 1s spectra obtained for metallic and strongly-oxidized Ni_{ED}/C samples after their treatment in either 1 M NaOH or 1 M NaOH + 50 mM $NaBH_4$. Ni $2p_{3/2}$ spectra were curve-fitted with Ni^0 (gray) and NiO_x (green, labeled as Ni^{2+} in the panels) components, their resulting atomic concentrations are indicated in corresponding panels.

To clarify whether the interference from the competing HER could be alleviated by controlling the oxidation state of surface of Ni, the extent of oxidation of Ni nanoparticles was purposely varied and three types of electrodes were considered: (i) strongly-oxidized Ni_{ED}/C, *i.e.* the sample subjected to potential cycling in a wide potential interval from -0.2 to 1.6 V *vs* RHE as it is typically done in the literature; (ii) partially-oxidized Ni_{ED}/C, *i.e.* the sample subjected to

electrochemical oxidation at 1.0 V *vs* RHE and (iii) metallic Ni_{ED}/C, which was studied right after preparation, without application of potentials above 0.5 V *vs* RHE. For further details regarding the sample preparation the reader is referred to the Supporting Information. Oxidation of Ni_{ED}/C results in a decrease of the ECSA from 93.4 to 52.5 and 25.9 $m^2\ g_{Ni}^{-1}$ for metallic, partially-, and strongly-oxidized Ni_{ED}/C electrodes, respectively (Figure S4), which reflects the number of available Ni metal sites on the electrode surface. The latter is further confirmed by XPS characterization of metallic and strongly-oxidized Ni_{ED}/C electrodes performed after their cycling in 1 M NaOH electrolyte (Figures 1d, e). Note however that due to *ex situ* character of the XPS analysis one cannot exclude that a part of Ni^{2+} species was formed during the sample transfer to the XPS chamber.

Figure 2 and S5 indicate that, indeed, the extent of the surface oxidation has a major influence on the BOR. Strongly-oxidized Ni_{ED}/C shows the lowest BOR activity, while reduced Ni_{ED}/C demonstrates the highest activity. We should emphasize that once Ni is oxidized at very high anodic potentials (> 1.3 V *vs* RHE) its reduction becomes impossible even in the presence of 50 mM $NaBH_4$, as it is clearly seen from the comparison of Ni 2p spectra obtained for strongly-oxidized Ni_{ED}/C (Figure 1d).

The extraordinary activity of the metallic Ni_{ED}/C can be attributed to the sluggish kinetics of the competing HER, which is evidenced by small cathodic currents in Figure 2a. In agreement with previous findings [24,27,35], the HER current increases several times on the partially-oxidized Ni_{ED}/C electrode (Figure 2a), due to a decrease of the hydrogen binding-energy on the Ni surface in the presence of closely-located Ni oxide species [26,43]. This HER increase translates in a significant decrease of the BOR currents and a positive shift of the OCP (open-circuit potential). Interestingly, the BOR and the HER currents are not in direct anti-correlation (*cf.* Figure 2a,b) suggesting a

complex interplay between the adsorption energies, the Ni site availability and the electrochemical kinetics of BOR/HER. The onset-potential for the oxidation of 5 mM $NaBH_4$ is -0.052 V *vs* RHE for strongly-oxidized Ni_{ED}/C, while it shifts favorably to -0.152 V *vs* RHE and -0.235 V *vs* RHE in the case of partially-oxidized and metallic Ni_{ED}/C electrodes, respectively (Table 1). To sum up, by suppressing the rate of electrochemical HER and increasing the metallic character of the Ni surface, we significantly improve the performance of Ni electrocatalyst in the BOR (Figure 2b). In particular, metallic Ni_{ED}/C demonstrates the highest BOR current densities measured at 0.1 V *vs* RHE, being *ca.* 1.5 and *ca.* 15 times larger compared to partially- and strongly-oxidized Ni_{ED}/C, respectively (Figure 2c). The current densities of metallic Ni_{ED}/C sample measured below 0.3 V *vs* RHE, in both potentiostatic and potentiodynamic modes, were much larger compared to any Ni-based electrocatalysts (including those consisting of noble metals) published in the literature (Table S2). Thus, the surface state of Ni is of paramount importance for its BOR activity, which accounts for the contradictory conclusions in the literature regarding the BOR at Ni, since the oxidation state of Ni surfaces has not been controlled in previously published measurements [28–34,44]. In this respect, it is extremely important to avoid applying anodic potentials higher than 0.3 V *vs* RHE, during electrokinetic studies of the BOR on Ni-based materials. Applying higher potentials leads to continuous passivation of the Ni electrode surface, resulting in rapid decrease of the BOR activity of metallic Ni_{ED}/C (Figure S6).

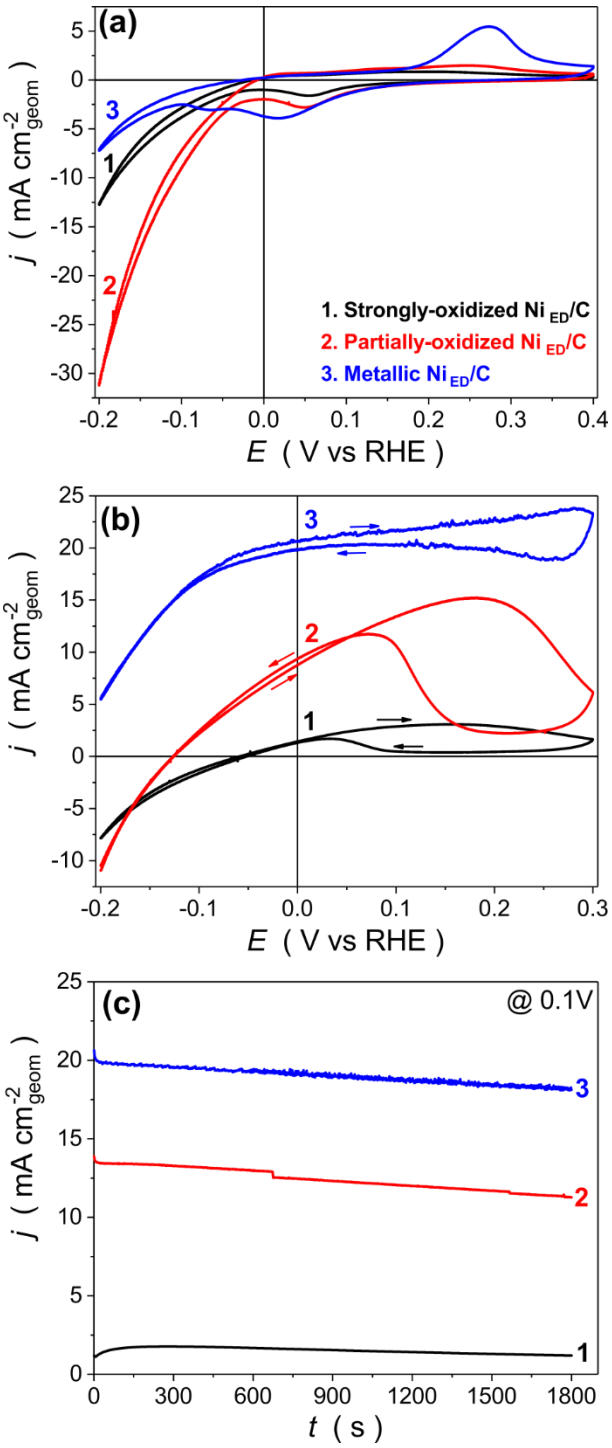

Figure 2. (a, b) CV and (c) chronoamperometry curves obtained for various Ni_{ED}/C rotating disc electrodes (RDE) under N_2 atmosphere at the following conditions: (a) 1.0 M NaOH, v = 20 mV

s^{-1}, ω = 0 rpm, (b) 1.0 M NaOH + 5 mM $NaBH_4$, v = 20 mV s^{-1}, ω = 1600 rpm, (c) 1.0 M NaOH + 5 mM $NaBH_4$, ω = 1600 rpm, E = 0.1 V vs RHE.

Table 1. Comparison of kinetic parameters for various carbon-supported metal electrocatalysts in the BOR.

Electrocatalyst	Half-cell open-circuit potential / RDE (V vs RHE)		Electrocatalyst	Unit-cell open-circuit voltage / DBFC (V)	
	5 mM BH_4^-	50 mM BH_4^-		50 mM BH_4^-	500 mM BH_4^-
Strongly-oxidized Ni_{ED}/C	-0.052		Ni_{ED}/GDE-L	1.10	1.18
Partially-oxidized Ni_{ED}/C	-0.152		Ni_{ED}/GDE-H		1.21
Metallic Ni_{ED}/C	-0.235	-0.258	Pt-black/GDE		1.03
Pt/C	-0.041	-0.051			
Pd/C	-0.140	-0.189			
Au/C	-0.121	-0.015			

Comparison of Ni_{ED}/C with noble metal electrocatalysts. The BOR activity of metallic Ni_{ED}/C is compared with the commercially-available 40 wt. % Pt/C, Pd/C and Au/C electrocatalysts – the benchmarks in the field. Two concentrations of $NaBH_4$ solution, 5 and 50 mM, in 1.0 M NaOH, were chosen to compare the electrocatalysts, to evaluate the influence of electrode surface-poisoning by boron-containing species. The measurements were performed under potentiodynamic and potentiostatic conditions in the potential range between $-0.2 < E < 0.3$ V *vs* RHE, as larger potentials are not attractive for a practical application (they would correspond to a low DBFC voltage). Potentiodynamic measurements (Figure 3a,b) evidence unmatched activity for Ni_{ED}/C at potentials below 0 V *vs* RHE, both in 5 and 50 mM $NaBH_4$ solution.

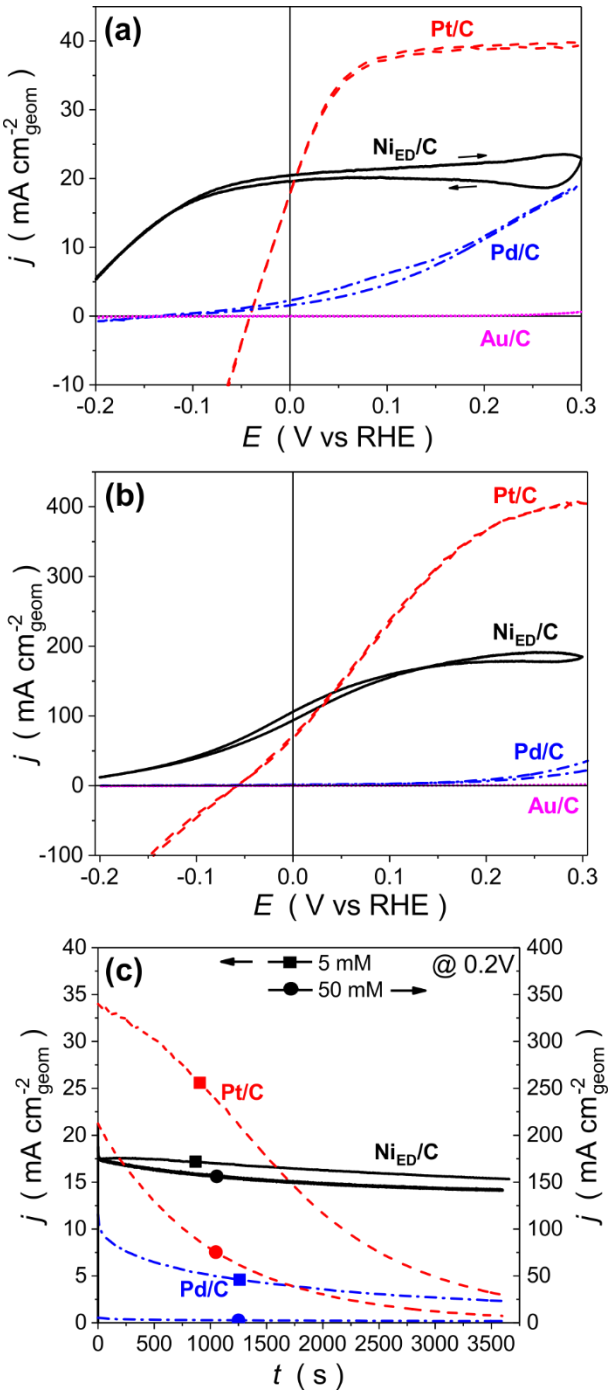

Figure 3. CV curves obtained for metallic Ni_{ED}/C (solid curve), Pt/C (dashed curve), Pd/C (dash-dotted curve) and Au/C (dotted curve) in N_2-saturated 1.0 M NaOH + 5 (a) or 50 (b) mM $NaBH_4$ at v = 20 mV s^{-1} and ω = 1600 rpm. (c) Potentiostatic measurement of the corresponding electrodes at E = 0.2 V vs RHE.

Metallic Ni_{ED}/C exhibits positive currents even at E = -0.2 V *vs* RHE (Figures 3a,b, S7), while for Pt/C, the high rate of the HER limits the efficiency of the BOR below 0 V *vs* RHE. The same is true for Pd/C, though to a lesser extent. Mass-transport-limited current densities can be reached at more anodic potentials, but (in the studied potential window) only for the Pt/C and Ni_{ED}/C electrocatalysts. An increase of the BH_4^- concentration requires higher applied potentials to reach the limiting current. The rotation rate dependence (Figure S8) allows us to estimate the number of electrons involved in the BOR as *ca*. 4 and 6 for Ni_{ED}/C and Pt/C, respectively; the difference likely originates from different BOR mechanisms (*cf* Computational modeling) on these metals and/or from the ability of Pt to oxidize hydrogen evolved during the oxidation/hydrolysis of borohydride. An impact of the HOR on metallic Ni becomes visible only above E = 0.2 V *vs* RHE, just before the onset of passivation of the electrode surface by (hydr)oxide species (Figures 3, S8) in agreement with Oshchepkov et al. [25]. Finally, the activity of Pd/C and Au/C is much smaller than for Ni_{ED}/C and Pt/C in the studied potential range, especially at 50 mM $NaBH_4$.

While potentiodynamic measurements show higher BOR currents on Pt compared to Ni above E = 0.2 V *vs* RHE, potentiostatic measurements (Figure 3c) reveal that the BOR activity of Pt is unstable and promptly decays, the loss exceeding 90 % after only 1 hour. A similar decrease, although to lesser extent, was observed for Pd/C, with *ca*. 80 % current decay after 1 hour, while Au/C is almost inactive at potentials below 0.3 V *vs* RHE (Figure S9). Contrary to the Pt/C and Pd/C electrocatalysts, the activity of Ni_{ED}/C is relatively stable with only *ca*. 12 and 18 % current decay after 1 hour at 5 and 50 mM $NaBH_4$, respectively. Besides, the BOR currents on Ni_{ED}/C are almost proportional to the concentration of $NaBH_4$, whereas the BOR performances of the Pt/C and Pd/C electrocatalysts at higher $NaBH_4$ concentrations are worse than expected (Figures 3c). To some extent, the current decay on Ni_{ED}/C is related to the poisoning of Ni active sites by the

formed Ni-B and B^{3+} species as evidenced from the XPS analysis (Figure S10, Table S1). However, no modification in the size/shape of the Ni nanoparticles after the treatment in borohydride electrolyte was found compared to the Ni nanoparticles obtained right after their synthesis by electrodeposition (TEM images on Figure S11), which demonstrates to some extent the robustness of these materials.

The effect of poisoning becomes more important below E = 0 V *vs* RHE, with an ability of Ni to regenerate active surface sites already at 0.1 V *vs* RHE (Figure S7), while noble metals require application of much larger potentials. Poisoning and likely mass-transport limitations become more important at high concentrations of $NaBH_4$, resulting in a decrease of the concentration-normalized current densities of Ni_{ED}/C (Figure S12), as was previously shown for Pt, Pd and Au massive electrodes [6]. Meanwhile, higher stability of the BOR currents on Ni_{ED}/C over Pt/C and Pd/C electrocatalysts is related to a weaker adsorption of poisoning boron species on the surface of Ni as discussed below (*cf* Computational modeling).

Fuel cell performance. Electrodeposited Ni was further evaluated in a unit DBFC. For this, Ni particles were deposited directly on a carbon cloth at low (Ni_{ED}/GDE-L, 0.60 ± 0.05 mg_{Ni} cm^{-2}) or high (Ni_{ED}/GDE-H, 3.6 ± 0.1 mg_{Ni} cm^{-2}) metal loading and compared with commercial Pt-black/GDE anode. Separated metal particles consisting of smaller crystallites were mainly found in Ni_{ED}/GDE-L (Figures 4c, e, S13), while in the Ni_{ED}/GDE-H electrode, Ni particles fully cover the external surface of the support (Figures 4d, f). The size of Ni crystallites was estimated from XRD patterns as 13.4 and 16.3 nm for Ni_{ED}/GDE-L and Ni_{ED}/GDE-H, respectively. Unit DBFCs using Pt-black/GDE and Ni_{ED}/GDE anodes displayed open-circuit voltages of $U_{j=0}$ = 1.0 and 1.2 V, respectively (Table 1), thus reflecting the difference observed in RDE studies for Pt/C and Ni_{ED}/C samples. More importantly, the cell with Ni_{ED}/GDE-L anode significantly outperforms the

Elrespectively, Figure 4g). Remarkably, relatively high and stable current densities were obtained for the first time at cell voltages as high as 1.0 V using Ni_{ED}/GDE anodes (Figure 4h), *i.e*. the voltage at which noble metals are not able to oxidize BH_4^-. Again, we emphasize that the reduced state of the Ni surface is the key factor for the high performance of a DBFC. For this reason, the cell voltage should not be lowered below U = 0.5 V during the test, to avoid irreversible Ni oxidation and ensure repeatable results. Deliberate partial oxidation of Ni_{ED}/GDE either electrochemically or under prolonged contact with air results in *ca.* 12% decrease of the performance, respectively (Figure S14). Operation of DBFCs with Ni anodes at high voltages would also be better in avoiding secondary H_2 evolution, for which the rate increases with a decrease of cell voltage (Figure S15). It is well known that H_{ad} is strongly adsorbed on metallic Ni which results in "low" HER (both from water and BH_4^-) at high voltages. However when anodic potential increases (cell voltage decreases) the strength of Ni-H_{ad} bond becomes lower, thus stimulating the HER, since formation of adsorbed H_{ad} (at these potentials) mainly proceeds through the dissociation of BH_4^- molecule and not from H_2O. When Pt is used at the anode of a DBFC, the production of hydrogen instead decreases at lower cell voltages (Figure S15), due to high activity of Pt in the HOR. Surprisingly, both Ni_{ED}/GDE-L and Ni_{ED}/GDE-H show similar performance (Figure 4g), despite a 6-fold difference in the Ni-loading. This suggests that the high-performing Ni-based DBFCs may be limited by either (i) the cathode used, (ii) partial operation of the anode or (iii) the construction of the cell; this effect was not observed for (lower-performances) Pt-based DBFCs.

Although additional studies are necessary to optimize the preparation parameters of the membrane electrode assembly with Ni_{ED} electrocatalysts, DBFCs with Ni_{ED}/GDE anodes already show great promise and outperform DBFCs with Pt anodes in terms of maximum power density

normalized by the mass of the active anode component (Table S2). Besides, they show better performance compared to hydrogen-fed alkaline membrane FC (AMFC) with state-of-the-art PGM-free anode electrocatalyst NiMo/KB [45]. The latter system shows power density around P = 120 mW cm^{-2} at j = 0.22 A cm^{-2}, while it is as high as P = 155 mW cm^{-2} at the same current density for a DBFC with Ni$_{ED}$/GDE-L anode, although lower metal loading and operating temperature were used in the latter case (0.6 *vs* 2 mg cm^{-2} and 60 *vs* 70ºC for DBFC with Ni$_{ED}$/GDE and AMFC with NiMo/KB, respectively).

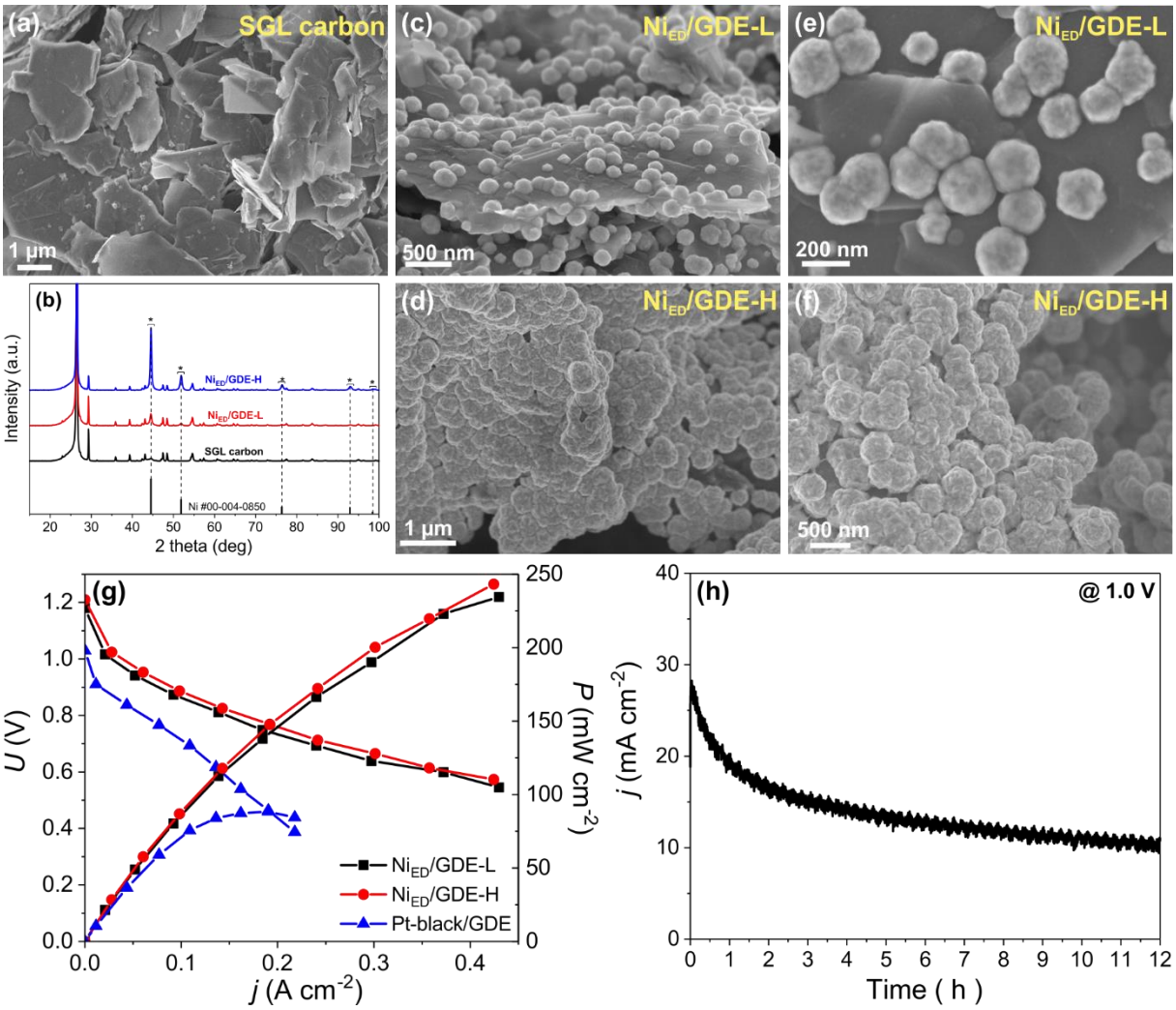

Figure 4. Characterization of Ni$_{ED}$/GDE samples. SEM images of pure SGL carbon (a) and after electrodeposition of Ni nanoparticles at low (Ni$_{ED}$/GDE-L, c and e) and high (Ni$_{ED}$/GDE-H, d and

f) metal loading; (c) XRD patterns obtained for the corresponding samples; (g) Ohmic-drop corrected I-U and I-P curves registered in fuel cell configuration using either Ni_{ED}/GDE or Pt-black/GDE anodes and Pt-black/GDE cathode; (h) Durability study of Ni_{ED}/GDE-H anode at the potentiostatic hold at 1.0 V.

Computational modelling by DFT and electrocatalyst design principles. To better understand the superior performance of Ni electrocatalysts in the BOR, DFT calculations were used to determine the binding energies of key species on the Ni (111) surface and compare them with those published for Pt (111), Au (111) and Pd (111) surfaces. Differences among these metals are apparent in the initial adsorption and B-H dissociation of BH_4^-. As Table 2 shows, the binding of borohydride varies from strong on Pt to weak on Au surfaces, with Pd and Ni metals having intermediate values. The inability of Au to break B-H bonds at low BOR overpotentials [5,7,46] makes this metal inappropriate for practical applications. On the Pt (111) surface, the adsorption of BH_4^- species is detrimentally-strong, adsorbing dissociatively, with no barrier for B-H bond breaking [47]. This leads to fast poisoning of Pt active sites with BH* species (likely responsible for the current decay for Pt/C in Figure 3c) and formation of H* that contributes to the non-selective H_2 evolution. Oxidation of the BH* species resulting from BH_4^- dissociation is slow on Pt at potentials below 0 V *vs* RHE, resulting in slow BOR kinetics [8,47]. The interaction of BH_4* with the Ni surface is intermediate to that of Au and Pt. The binding is strong-enough to allow for subsequent oxidation, but not too strong to lead to surface poisoning. DFT calculations predict molecular (non-dissociative) adsorption of BH_4^- on the Ni (111) surface, although the stretching of the B-H bond suggests facile dissociation. B-H bond dissociation is further promoted by strong adsorption of formed H* on the surface of pure Ni. Although the detailed data regarding adsorption of various

BH_xO_y species are not included for the Pd surface, the electrochemical results point to a similar behavior than for Pt surface.

Subsequent reaction steps also suggest the complete borohydride oxidation process can occur at low overpotentials on Ni (111), and via an alternative mechanism than found on Pt (111). Binding of the BH* species is weaker on the Ni (111) surface compared to the Pt (111) surface. Alternatively, BH_2OH* binds stronger to the Ni (111) surface compared to the Pt (111) surface, causing B-OH bond formation to precede complete B-H dissociation, as BH_2OH* is the significantly-preferred 4-electron intermediate, compared to BH*, on Ni (111), in agreement with the experimental data. The reaction energy for BH_4* conversion to BH* and BH_2OH* is calculated on the Ni (111) surface at 0 V *vs* RHE:

$$BH_4^* + 3OH^- \rightarrow BH_2OH^* + 2H_2O + 3e^- \qquad \Delta G = \text{-0.47 eV} \qquad (5)$$

$$BH_4^* + 3OH^- \rightarrow BH^* + 3H_2O + 3e^- \qquad \Delta G = \text{+0.17 eV} \qquad (6)$$

Therefore, unlike the Pt (111) surface, the Ni (111) surface will not be poisoned by BH* species at low potentials, suggesting that Ni (111) can outperform Pt (111) below E = 0 V *vs* RHE. The expected higher coverage of OH* on Ni (111) at BOR-relevant potentials (see stronger OH* binding in Table 2) will also help to promote B-OH bond formation.

The HER competes with the BOR for E < 0 V *vs* RHE. The weaker binding of H* on Pt (relative to Ni) results in intensive H_2 escape, while H* adsorption is very strong on metallic Ni [43], which explains its low activity in the HER. Based on DFT results, the BOR on Ni (111) is expected to be faster than on Pt (111) at low potentials, though one cannot differentiate whether this is the leading cause of the observed higher oxidation current on Ni at low potentials, rather than the lower competing reduction current for the HER on Ni.

Table 2 Binding energies of species bound to the M (111) surface at optimal binding sites.

Species	Binding energy (eV)			
	Ni (111)	Pt (111)	Au (111)	Pd (111)
BH_4*	-3.68; -3.50 [9]	-	-1.73 [46]; -1.96 [9]	-
BH+3H*	-	-4.73 [47]; -4.56 [9]	-	-3.63 [9]
BH_3*	-2.19	-1.94 [47]	-0.55 [46]	
BH_2*	-4.10	-3.40 [47]	-2.64 [46]	
BH*	-5.39	-6.14 [47]	-4.40 [46]	
B*	-5.75	-6.50 [47]	-4.43 [46]	
BH_3OH*	-2.77		-1.08 [46]	
BH_2OH*	-1.27	-0.06 [47]	-0.06 [46]	
BHOH*	-3.46	-3.31 [47]	-2.34 [46]	
BOH*	-3.74	-4.41 [47]	-2.76 [46]	
$BH(OH)_2$*	-0.49	-0.17 [47]	-0.05 [46]	
$B(OH)_2$*	-2.36	-3.09 [47]	-2.20 [46]	
$B(OH)_3$*	-0.22	-0.16 [47]		
H*	-2.86; -2.94 [48]	-2.72 [47]; -2.72 [48]	-2.12 [46]; -2.18 [48]	-2.88 [48]
OH*	-3.37; -3.42 [49]	-2.26 [47]; -2.34 [49]	-1.79 [46]; -2.21 [49]	-2.62 [49]
H_2O*	-0.30; -0.33 [49]	-0.25 [47]; -0.29 [49]	-0.11 [46]; -0.12 [49]	-0.30 [49]

CONCLUSION

Carbon-supported Ni nanoparticles prepared via an easily-scalable electrochemical deposition process demonstrate an outstanding activity in the BOR at potentials below E = 0 V *vs* RHE and

outperform all the noble-metal electrocatalysts tested as benchmarks under the same conditions. The experimental data reveal that controlling the surface oxidation state rgreatly impacts the activity of Ni in the BOR; the highest activity is measured for reduced metallic Ni, and substantially drops after partial oxidation of the electrode surface. Experimental data reinforced by DFT calculations suggest that a good electrocatalyst enabling the BOR at low overpotentials should allow: (i) dissociative but not too strong BH_4^- adsorption, (ii) relatively strong adsorption of H_{ad} (to decrease the HER) and (iii) formation of OH_{ad} species at low potentials (to enable the oxidation of poisoning B-containing species).

ASSOCIATED CONTENT

Supporting Information. Details of the preparation of Ni_{ED}/C electrocatalysts, calculation of electrochemical surface area of Ni_{ED}/C, reduction treatment of oxidized Ni_{ED}/C, potentiostatic measurements of Ni_{ED}/C and Pt/C in RDE configuration, analysis of RDE plots for Ni_{ED}/C and Pt/C, voltammetric and potentiostatic measurements of Au/C, TEM images for Ni_{ED}/GDE-L and Fuel Cell performances of fresh and oxidized Ni_{ED}/GDE-L, details of XPS analysis of Ni_{ED}/C electrocatalysts, tables with comparison of performances of various BOR electrocatalysts in either three-electrode cell or DBFC configurations.

AUTHOR INFORMATION

Corresponding Author

* E-mail: Oshchepkov@catalysis.ru

* E-mail: Marian.Chatenet@grenoble-inp.fr

Author Contributions

AO, GB and SOA contributed to the experimental work, data analysis and writing of the manuscript.

GR and MJJ performed the DFT calculations and contributed to the writing of the manuscript.

VP performed XPS analysis and contributed to the writing of the manuscript.

GM, AB, ERS and MC contributed to the project planning, experimental work, data analysis, writing and review of the manuscript.

Notes

The authors declare no financial and non-financial competing interests.

ACKNOWLEDGMENTS

This work has been performed in the frame of the MobiDiC project, funded by the French National Research Agency (ANR, grant No. ANR-16-CE05-0009-01) and RSF project No. 18-73-00143, funded by the Russian Science Foundation. Some of the work presented herein has been performed within the framework of the Centre of Excellence of Multifunctional Architectured Materials "CEMAM" No. ANR-10-LABX-44-01. The authors express their gratitude to Dr. C. Ulhaq-Bouillet, Dr. T. Dintzer and Dr. A. Boss for their assistance with (S)TEM, SEM and ICP-AES analysis, and to Prof. U. Demirci for fruitful discussions.

REFERENCES

(1) Ma, J.; Choudhury, N. A.; Sahai, Y. A Comprehensive Review of Direct Borohydride Fuel Cells. *Renew. Sustain. Energy Rev.* **2010**, *14*, 183–199.

(2) Wang, Z.; Parrondo, J.; He, C.; Sankarasubramanian, S.; Ramani, V. Efficient PH-Gradient-Enabled Microscale Bipolar Interfaces in Direct Borohydride Fuel Cells. *Nat. Energy* **2019**,

4, 281–289.

(3) Dekel, D. R. Review of Cell Performance in Anion Exchange Membrane Fuel Cells. *J. Power Sources* **2018**, *375*, 158–169.

(4) Olu, P. Y.; Job, N.; Chatenet, M. Evaluation of Anode (Electro)Catalytic Materials for the Direct Borohydride Fuel Cell: Methods and Benchmarks. *J. Power Sources* **2016**, *327*, 235–257.

(5) Olu, P. Y.; Bonnefont, A.; Braesch, G.; Martin, V.; Savinova, E. R.; Chatenet, M. Influence of the Concentration of Borohydride towards Hydrogen Production and Escape for Borohydride Oxidation Reaction on Pt and Au Electrodes – Experimental and Modelling Insights. *J. Power Sources* **2018**, *375*, 300–309.

(6) Braesch, G.; Bonnefont, A.; Martin, V.; Savinova, E. R.; Chatenet, M. Borohydride Oxidation Reaction Mechanisms and Poisoning Effects on Au , Pt and Pd Bulk Electrodes : From Model (Low) to Direct Borohydride Fuel Cell Operating (High) Concentrations. *Electrochim. Acta* **2018**, *273*, 483–494.

(7) Finkelstein, D. A.; Letcher, C. D.; Jones, D. J.; Sandberg, L. M.; Watts, D. J.; Abruña, H. D. Self-Poisoning during BH_4^- Oxidation at Pt and Au, and in Situ Poison Removal Procedures for BH_4^- Fuel Cells. *J. Phys. Chem. C* **2013**, *117*, 1571–1581.

(8) Rostamikia, G.; Janik, M. J. Direct Borohydride Oxidation: Mechanism Determination and Design of Alloy Catalysts Guided by Density Functional Theory. *Energy Environ. Sci.* **2010**, *3*, 1262–1274.

(9) Escaño, M. C. S. Borohydride Electro-Oxidation on Metal Electrodes: Structure, Composition and Solvent Effects from DFT. *SPR Electrochem.* **2017**, *14*, 1–22.

(10) Escaño, M. C. S.; Arevalo, R. L.; Gyenge, E.; Kasai, H. Electrocatalysis of Borohydride

Oxidation: A Review of Density Functional Theory Approach Combined with Experimental Validation. *J. Phys. Condens. Matter* **2014**, *26*, 353001.

(11) Merino-Jiménez, I.; Ponce De León, C.; Shah, A. A.; Walsh, F. C. Developments in Direct Borohydride Fuel Cells and Remaining Challenges. *J. Power Sources* **2012**, *219*, 339–357.

(12) Ouyang, L.; Huang, J.; Wang, H.; Liu, J.; Zhu, M. Progress of Hydrogen Storage Alloys for Ni-MH Rechargeable Power Batteries in Electric Vehicles : A Review. *Mater. Chem. Phys.* **2017**, *200*, 164–178.

(13) Salunkhe, R. R.; Lin, J.; Malgras, V.; Xue, S.; Ho, J.; Yamauchi, Y. Large-Scale Synthesis of Coaxial Carbon Nanotube/$Ni(OH)_2$ Composites for Asymmetric Supercapacitor Application. *Nano Energy* **2015**, *11*, 211–218.

(14) Cao, F.; Pan, G. X.; Xia, X. H.; Tang, P. S.; Chen, H. F. Synthesis of Hierarchical Porous NiO Nanotube Arrays for Supercapacitor Application. *J. Power Sources* **2014**, *264*, 161–167.

(15) Zhang, M.; Huang, Z.; Shen, Z.; Gong, Y.; Chi, B.; Pu, J.; Li, J. High-Performance Aqueous Rechargeable Li-Ni Battery Based on $Ni(OH)_2$/NiOOH Redox Couple with High Voltage. *Adv. Energy Mater.* **2017**, *7*, 1700155.

(16) Yuan, C.; Wu, H. Bin; Xie, Y.; Lou, X. W. Mixed Transition-Metal Oxides: Design, Synthesis, and Energy-Related Applications Changzhou. *Angew. Chemie Int. Ed. English* **2014**, *53*, 1488–1504.

(17) Li, W.; Song, B.; Manthiram, A. High-Voltage Positive Electrode Materials for Lithium-Ion Batteries. *Chem. Soc. Rev.* **2017**, *46*, 3006–3059.

(18) Roger, I.; Shipman, M. A.; Symes, M. D. Earth-Abundant Catalysts for Electrochemical and Photoelectrochemical Water Splitting. *Nat. Rev. Chem.* **2017**, *1*, 0003.

(19) Song, F.; Hu, X. Exfoliation of Layered Double Hydroxides for Enhanced Oxygen Evolution Catalysis. *Nat. Commun.* **2014**, *5*, 4477.

(20) Zhao, Q.; Yang, J.; Liu, M.; Wang, R.; Zhang, G.; Tang, H.; Liu, C.; Mei, Z.; Chen, H.; Pan, F. Tuning Electronic Push/Pull of Ni-Based Hydroxides to Enhance Hydrogen and Oxygen Evolution Reactions for Water Splitting. *ACS Catal.* **2018**, *8*, 5621–5629.

(21) Schalenbach, M.; Kasian, O.; Mayrhofer, K. J. J. An Alkaline Water Electrolyzer with Nickel Electrodes Enables Efficient High Current Density Operation. *Int. J. Hydrogen Energy* **2018**, *43*, 11932–11938.

(22) Diaz-Morales, O.; Ledezma-Yanez, I.; Koper, M. T. M.; Calle-Vallejo, F. Guidelines for the Rational Design of Ni-Based Double Hydroxide Electrocatalysts for the Oxygen Evolution Reaction. *ACS Catal.* **2015**, *5*, 5380–5387.

(23) McCrory, C. C. L.; Jung, S.; Peters, J. C.; Jaramillo, T. F. Benchmarking Heterogeneous Electrocatalysts for the Oxygen Evolution Reaction. *J. Am. Chem. Soc.* **2013**, *135*, 16977–16987.

(24) Gong, M.; Wang, D.-Y. Y.; Chen, C.-C. C.; Hwang, B.-J. J.; Dai, H. A Mini Review on Nickel-Based Electrocatalysts for Alkaline Hydrogen Evolution Reaction. *Nano Res.* **2016**, *9*, 28–46.

(25) Oshchepkov, A. G.; Bonnefont, A.; Pronkin, S. N.; Cherstiouk, O. V.; Ulhaq-Bouillet, C.; Papaefthimiou, V.; Parmon, V. N.; Savinova, E. R. Nanostructured Nickel Nanoparticles Supported on Vulcan Carbon as a Highly Active Catalyst for the Hydrogen Oxidation Reaction in Alkaline Media. *J. Power Sources* **2018**, *402*, 447–452.

(26) Wang, J.; Mao, S.; Liu, Z.; Wei, Z.; Wang, H.; Chen, Y.; Wang, Y. Dominating Role of Ni ^{0} on the Interface of Ni/NiO for Enhanced Hydrogen Evolution Reaction. *ACS Appl. Mater.*

Interfaces **2017**, *9*, 7139–7147.

(27) Danilovic, N.; Subbaraman, R.; Strmcnik, D.; Chang, K. C.; Paulikas, A. P.; Stamenkovic, V. R.; Markovic, N. M. Enhancing the Alkaline Hydrogen Evolution Reaction Activity through the Bifunctionality of $Ni(OH)_2$/Metal Catalysts. *Angew. Chemie - Int. Ed.* **2012**, *51*, 12495–12498.

(28) Ma, X.; Ye, K.; Wang, G.; Duan, M.; Cheng, K.; Wang, G.; Cao, D. Facile Fabrication of Gold Coated Nickel Nanoarrays and Its Excellent Catalytic Performance towards Sodium Borohydride Electro-Oxidation. *Appl. Surf. Sci.* **2017**, *414*, 353–360.

(29) Li, S.; Shu, C.; Chen, Y.; Wang, L. A New Application of Nickel-Boron Amorphous Alloy Nanoparticles: Anode-Catalyzed Direct Borohydride Fuel Cell. *Ionics* **2018**, *24*, 201–209.

(30) Zhang, D.; Wang, G.; Yuan, Y.; Li, Y.; Jiang, S.; Wang, Y.; Ye, K.; Cao, D.; Yan, P.; Cheng, K. Three-Dimensional Functionalized Graphene Networks Modified Ni Foam Based Gold Electrode for Sodium Borohydride Electrooxidation. *Int. J. Hydrogen Energy* **2016**, *41*, 11593–11598.

(31) Dong, H.; Feng, R.; Ai, X.; Cao, Y.; Yang, H.; Cha, C. Electrooxidation Mechanisms and Discharge Characteristics of Borohydride on Different Catalytic Metal Surfaces. *J. Phys. Chem. B* **2005**, *109*, 10896–10901.

(32) Geng, X.; Zhang, H.; Ye, W.; Ma, Y.; Zhong, H. Ni-Pt/C as Anode Electrocatalyst for a Direct Borohydride Fuel Cell. *J. Power Sources* **2008**, *185*, 627–632.

(33) Zhang, D.; Cheng, K.; Shi, N.; Guo, F.; Wang, G.; Cao, D. Nickel Particles Supported on Multi-Walled Carbon Nanotubes Modified Sponge for Sodium Borohydride Electrooxidation. *Electrochem. commun.* **2013**, *35*, 128–130.

(34) Santos, D. M. F.; ljuki , B.; Amaral, L.; Maccio, D.; Saccone, A.; Sequeira, C. A. C. Nickel

and Nickel-Cerium Alloy Anodes for Direct Borohydride Fuel Cells. *J. Electrochem. Soc.* **2014**, *161*, F594–F599.

(35) Oshchepkov, A. G.; Bonnefont, A.; Saveleva, V. A.; Papaefthimiou, V.; Zafeiratos, S.; Pronkin, S. N.; Parmon, V. N.; Savinova, E. R. Exploring the Influence of the Nickel Oxide Species on the Kinetics of Hydrogen Electrode Reactions in Alkaline Media. *Top. Catal.* **2016**, *59*, 1319–1331.

(36) Olu, P. Y.; Deschamps, F.; Caldarella, G.; Chatenet, M.; Job, N. Investigation of Platinum and Palladium as Potential Anodic Catalysts for Direct Borohydride and Ammonia Borane Fuel Cells. *J. Power Sources* **2015**, *297*, 492–503.

(37) Mainka, J.; Maranzana, G.; Dillet, J.; Didierjean, S.; Lottin, O. On the Estimation of High Frequency Parameters of Proton Exchange Membrane Fuel Cells via Electrochemical Impedance Spectroscopy. *J. Power Sources* **2014**, *253*, 381–391.

(38) Kresse, G.; Furthmüller, J. Efficient Iterative Schemes for Ab Initio Total-Energy Calculations Using a Plane-Wave Basis Set. *Comput. Mater. Sci.* **1996**, *6*, 15–50.

(39) Kresse, G.; Furthmüller, J. Efficient Iterative Schemes for Ab Initio Total-Energy Calculations Using a Plane-Wave Basis Set. *Phys. Rev. B - Condens. Matter Mater. Phys.* **1996**, *54*, 11169–11186.

(40) Kresse, G.; Hafner, J. Ab Initio Molecular Dynamics for Liquid Metals. *Phys. Rev. B - Condens. Matter Mater. Phys.* **1993**, *47*, 558–561.

(41) Perdew, J. P.; Wang, Y. Accurate and Simple Analytic Representation of the Electron-Gas Correlation Energy. *Phys. Rev. B - Condens. Matter Mater. Phys.* **1992**, *45*, 13244–13249.

(42) Monkhorst, H. J.; Pack, J. D. Special Points for Brillonin-Zone Integrations. *Phys. Rev. B* **1976**, *13*, 5188–5192.

(43) Oshchepkov, A. G.; Bonnefont, A.; Parmon, V. N.; Savinova, E. R. On the Effect of Temperature and Surface Oxidation on the Kinetics of Hydrogen Electrode Reactions on Nickel in Alkaline Media. *Electrochim. Acta* **2018**, *269*, 111–118.

(44) Cheng, H.; Scott, K.; Lovell, K. Material Aspects of the Design and Operation of Direct Borohydride Fuel Cells. *Fuel Cells* **2006**, *6*, 367–375.

(45) Kabir, S. A.; Lemire, K.; Artyushkova, K.; Roy, A.; Odgaard, M.; Schlueter, D.; Oshchepkov, A.; Bonnefont, A.; Savinova, E.; Sabarirajan, D.; et al. Platinum Group Metal-Free NiMo Hydrogen Oxidation Catalysts: High Performance and Durability in Alkaline Exchange Membrane Fuel Cells. *J. Mater. Chem. A* **2017**, *5*, 24433–24443.

(46) Rostamikia, G.; Janik, M. J. Borohydride Oxidation over Au(111): A First-Principles Mechanistic Study Relevant to Direct Borohydride Fuel Cells. *J. Electrochem. Soc.* **2009**, *156*, B86.

(47) Rostamikia, G.; Janik, M. J. First Principles Mechanistic Study of Borohydride Oxidation over the Pt(111) Surface. *Electrochim. Acta* **2010**, *55*, 1175–1183.

(48) Ferrin, P.; Kandoi, S.; Nilekar, A. U.; Mavrikakis, M. Hydrogen Adsorption, Absorption and Diffusion on and in Transition Metal Surfaces: A DFT Study. *Surf. Sci.* **2012**, *606*, 679–689.

(49) Huang, S.-C.; Lin, C.-H.; Wang, J.-H. Trends of Water Gas Shift Reaction on Close-Packed Transition Metal Surfaces. *J. Phys. Chem. C* **2010**, *114*, 9826–9834.

TABLE OF CONTENTS

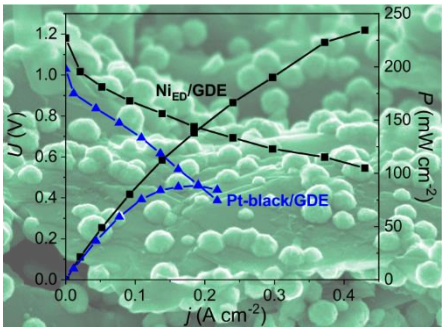
Ni$_{ED}$/GDE
Pt-black/GDE
U (V)
P (mW cm^{-2})
j (A cm^{-2})
0.0
0.2
0.4
0.6
0.8
1.0
1.2
0
50
100
150
200
250
0.1
0.3